Received: 30 January 2020 | Revised: 22 June 2020 | Accepted: 29 June 2020

DOI: 10.1002/eng2.12252

RESEARCH ARTICLE

WILEY

Process optimization of high entropy alloys by laser additive manufacturing

Modupeola Dada[1] | **Patricia Popoola**[1] | **Ntombi Mathe**[2] | **Sisa Pityana**[1,2] | **Samson Adeosun**[3] | **Olufemi Aramide**[1] | **Thabo Lengopeng**[1,2]

[1]Chemical, Metallurgical and Materials Engineering, Tshwane University of Technology, Pretoria, South Africa

[2]National Laser Center, Council for Scientific and Industrial Research, Pretoria, South Africa

[3]Metallurgical and Materials Engineering, University of Lagos, Akoka, Nigeria

Correspondence
Modupeola Dada, Chemical, Metallurgical and Materials Engineering, Tshwane University of Technology, Pretoria, South Africa.
Email: dadadupeola@gmail.com

Abstract

Aerospace components and their coatings are required to possess excellent surface properties over a wide temperature range. Stainless steels, titanium, nickel superalloy, and more recently high entropy alloys (HEAs) have been used to improve the exterior properties of these components. In this study, AlTiCrFeCoNi and AlCoCrFeNiCu HEAs were successfully fabricated using laser additive manufacturing to produce coatings on an A301 steel base plate. The influence of the laser parameters (laser power and scan speed) on the microstructure and hardness properties were also investigated. The results revealed that coatings homogeneously adhered to the baseplate. The optimum processing parameters for both alloys with defect-free structures at a preheat temperature of 400°C, were at 1200-1600 W at 8-12 mm/s with the layers composed of both face centred-cubic (FCC) and body centred-cubic (BCC) phases. The laser parameters affected the quality and hardness properties of the alloys. The results showed that optimizing the laser parameters achieved by preheating temperature invariably improved the performance of the alloys with potential coatings and structural applications.

KEYWORDS

additive manufacturing, high entropy alloys, laser coating, laser parameters

1 | INTRODUCTION

Manufacturing technologies are an important aspect of the industrial framework because, through them, fabrication of components for service industries such as; aerospace, energy, nuclear and automobile is accomplished.[1,2] These technologies can be categorized into traditional subtractive and formative, with newer technologies such as additive manufacturing.[3,4] Additive manufacturing (AM) is a process of joining materials to make parts from 3D model data, using layer upon layer.[5] This process is currently a preferred alternative to conventional manufacturing techniques owing to its many advantages such as its ability to manufacture complex parts using hard to machine materials such as titanium alloys.[6-8] There are several AM techniques classified by their energy source (arc, electron, and laser beam), method of feed material (powder bed, blown powder) and the feedstock (sheet, wire, or metal powder).[9,10] Laser additive

manufacturing (LAM) facilitates the fabrication of three-dimensional products with fewer defects through the optimization of its process parameters such as laser power, scanning speed.[9,10] The process is flexible, versatile, and customized, allowing for the manufacturing of more complex and intricate structures.[2,11] However, this technique can be susceptible to defects creating the need to optimize process parameters and improve the overall quality and properties of AM products.[12-14]

The laser energy source of AM has become an effective direct energy deposition method used in producing geometries with small heat-affected zones.[15,16] The direct energy deposition or powder blown method is used for creating coatings or cladding on the surface of a chosen substrate/baseplate as well as build up components.[17-19] The first set of materials used for systematic studies of LAM ranged from stainless steels, aluminum to nickel and titanium alloys,[20,21] however, due to the shortcomings of these materials; low strength at elevated temperatures, little or no corrosion and wear resistance to name a few, there has been a need to use other materials such as high entropy alloys. High entropy alloys (HEAs) are materials that are composed of at least five metallic components with a molar atomic concentration within a range of 5-35 at% .[22-24] Recently, HEAs are used and reported to be more durable, ductile, and flexible than some titanium and steel alloys .[23-25] Their excellent strength at elevated temperatures makes them potential materials for coatings in high temperature and corrosive environments, and refractory materials for aero-engine parts.[26-28]

Tong et al[29] synthesized $Al_xCoCrCuFeNi$ HEAs with molar ratio (x = 0-3.0) using casting and arc-melting method and the results indicated that the alloy's wear resistance was as high as that of SKD 61 steel. This was attributed to the excellent work hardening ability of the alloy. Kao et al[30] prepared the most studied AlxCoCrFeNi HEA using vacuum arc melting to investigate the magnetic, electrical, and thermal properties of the amalgam. The alloy showed a single FCC and a single BCC phase structure from X-ray diffraction studies, and there were no stress-induced phase transformations during deformation. The authors stated that the alloy's main strengthening mechanism is also work hardening and that the hardening ability of the alloy was twice in the FCC than in the BCC phase. Although these alloys are usually cast, there have been reports of oxides formation hindering the improvement of its mechanical properties caused by the manufacturing route adopted.[31]

In this case, alternative methods are required to fully take advantage of the benefits of HEAs. For instance, Zhou et al[32] fabricated HEAs using Selective Laser Melting (SLM); the authors reported that the SLM parameters influenced the density and the grain size of the alloys showing that improved properties can be achieved through the optimization of processing parameters. Jiang, et al[33] investigated the fabrication and characterization of AlCoCrFeNiNbx HEA coatings produced by laser cladding. The study revealed that the microstructures of the alloy transitioned from equiaxed grain to hypoeutectic, from hypoeutectic to full eutectic and then to hypereutectic as the composition of Nb varied from 0 to 0.75 at%, attributed to the cocktail effect of the alloys. Zhu et al[34] fabricated HEA using AM and they attributed the excellent ductility and high strength to the manufacturing process. The cellular structures obtained using SLM contributed to the strength via dislocation hardening while the ductility was achieved through strain hardening in the as-built samples compared with conventional methods. Popov et al[35] used elemental blends in fabricating HEA via selective electron beam melting and stated that the use of this processing route was less complicated than the powder metallurgy technique or other conventional methods. Also, when the parameters were not optimized, defects such as residual porosity were detected and the study recommended using heat treatment to get lower porosity levels. However, their emphasis was on the importance of optimizing the process parameters. On the other hand, Chao et al[36] produced AlxCoCrFeNi HEA by laser coating and stated that clads were defect-free with isothermal treatments at 1000°C and optimized process parameters with minimal dilution and an increase in the hardness values of the composition. Mahamood and Akinlabi[37] suggested using statistical modeling as an optimization tool and the authors argued that the method was cost-effective yet technical in nature. Aboutaleb et al[38] used experimental data from previous studies as an optimization tool and they reported that it was time and cost-effective however, the results also had to be verified through simulated modeling. Baturynska et al[39] also used simulation by finite element methodology and a machine learning technique as optimization tools stating that both methods were effective yet very technical. Popov et al[35] on the other hand, did not carry out optimization at first and noticed residual porosity after fabrication then the authors tried to use heat treatment as a post-optimization tool and they experienced undesirable compositional changes in their alloy.

According to Hofman,[40,41] the three most important processing parameters to ensure the quality of the alloys are the laser power, the scanning speed and the powder feed-rate.

The laser energy density given by Equation (1) is supplied by a laser beam in unit volume has a significant impact on the analysis of the microstructure and properties of materials.[42] There are three energy densities, namely; area, linear and volumetric.

According to Olakanmi et al,[43]

$$E = \frac{p}{v\,x\,d} \tag{1}$$

where p the laser power is in W, v is the laser scanning speed in mm/s, d is the beam diameter in mm and E is the laser energy density in J/mm^2.

These process parameters have the greatest influence on the overall quality and properties of the coatings. Serviceability of alloys manufactured using LAM also hinges on their microstructure and mechanical properties.[6,44,45] Laser deposition has been reported to be used for the production of end-use parts using titanium, nickel, and steel due to its many advantages over conventional methods, however, there are limited publications on the use and application of HEAs for aerospace structural applications using this technique. Since the desired performance of the LAM process depends primarily on its process parameters, the optimization of the process parameters is essential to achieve the desired properties of HEAs for aerospace applications. Most optimization studies using LAM did not use preheating temperature as an optimization tool. This study, therefore, proposes the use of preheat temperature as an optimization tool and investigates the effect of the variation of laser power, scan speed, and the concept of laser energy density on the microstructure, and hardness properties of AlCoCrFeNiCu and AlTiCrFeCoNi HEAs fabricated by LAM for aerospace applications.

2 | EXPERIMENTAL PROCEDURE

2.1 | Materials

Tables 1 and 2 show the chemical compositions of the AlCoCrFeNiCu (Cu-based) and AlTiCrFeCoNi (Ti-based) HEAs (16.6 at%) powder mixtures of Al, Co, Cr, Fe, Ni, Cu and Al, Ti, Cr, Fe, Co, Ni with purities above 99.9%. The powders were commercially supplied by F.J Brodmann & CO., L.L.C, USA, and they were used as-received without modification. Before deposition, the A301 steel baseplates were sandblasted to increase absorptivity of the laser beam and minimize reflection of the laser radiation; this improves the bonding strength between each alloy and the baseplate. After sandblasting, the surface of the baseplate was cleaned with acetone and air-dried before laser deposition to remove contaminants.

2.2 | Design of experiment

To achieve optimized process parameters, two stages of experiments were carried out using design of experiment {D.O.E} approach to develop different combinations of processing parameters as shown in Tables 3 and 4. Table 5 shows the laser process parameters used in this study as derived from the Design-Expert v11 software. The criteria for selecting the optimized parameters were centered on homogeneity in clad layer and defect-free microstructures using two factors, namely; laser power (P) and scan speed (mm/s) at three levels respectively.[46,47] The optimization tests were carried out varying the laser power from 600 to 1000 W at a scan speed from 4 to 12 mm/s for stage 1 of the experiment and 1200-1600 W at a scan speed of 8-12 mm/s for stage 2 while preheating the base plate at a constant rate of 400°C and constant powder feed rate, beam diameter, and layer thickness of 2 rpm, 2 mm, and 0.5 mm respectively. Using data from Table 5 and the design tool-STAT-EASE Inc. Design-Expert Software 11, surface plots were developed and displayed in Figures 10 and 11 to show the three-dimensional influence of laser parameters on the microhardness properties of the HEAs.

TABLE 1 Chemical composition of AlCoCrFeNiCu HEA

Element	Al (at%)	Co (at%)	Cr (at%)	Fe (at%)	Ni (at%)	Cu (at%)
Nominal	16.6	16.6	16.6	16.6	16.6	16.6
Cu-based HEA	42.95	11.09	10.24	13.52	10.36	11.84

TABLE 2 Chemical composition of AlTiCrFeCoNi HEA

Element	Al (at%)	Co (at%)	Cr (at%)	Fe (at%)	Ni (at%)	Ti (at%)
Nominal	16.6	16.6	16.6	16.6	16.6	16.6
Ti-based HEA	44.12	10.23	10.96	12.55	10.96	11.18

TABLE 3 Stage 1 of the experiment

Factors	Factor code	Level 1	Level 2	Level 3
Laser power (W)	A	600	800	1000
Scan speed (mm/s)	B	4	8	12

TABLE 4 Stage 2 of the experiment

Factors	Factor code	Level 1	Level 2	Level 3
Laser power (W)	A	1200	1400	1600
Scan speed (mm/s)	B	8	10	12

TABLE 5 Laser fabrication parameters

Laser power (P) (J/s) Factor A	Scan speed (V) (mm/s) Factor B	Beam diameter (mm)	Energy density ($E = P/V$*d) (J/mm^2)	Cu-based HEA microhardness Response 1	Ti-based HEA microhardness Response 2
600	4	2	75	552	684
600	8	2	37.5	542	778
600	12	2	25	579	811
800	4	2	100	542	689
800	8	2	50	583	699
800	12	2	33.3	587	782
1000	4	2	125	560	667
1000	8	2	62.5	521	650
1000	12	2	41.7	574	763
1200	8	2	75	389	380
1200	10	2	60	389	427
1200	12	2	50	700	433
1400	8	2	87.5	481	400
1400	10	2	70	617	456
1400	12	2	58.3	746	521
1600	8	2	100	597	380
1600	10	2	80	740	439
1600	12	2	66.7	837	466

The number of experiments is calculated by Equation (2)[48];

$$N = L^{\mathrm{F}} \tag{2}$$

where N is the number of experiments, F is the number of factors varied, and L is the number of the level set for the experiment. The final sets of 18 parameters used are shown in Table 5.

2.3 | Laser processing

The samples were prepared by melting the HEA powder onto a mild steel base plate using a 3 kW continuous wave ytterbium laser system, with a fitted robotic arm that moves in a multi-axial direction to control the process and a schematic representation of the laser-material deposition process is shown in Figure 1. The HEAs powder was delivered through a nozzle filled with argon as a carrier gas and fitted on the laser delivery head. To prevent time lag between the molten

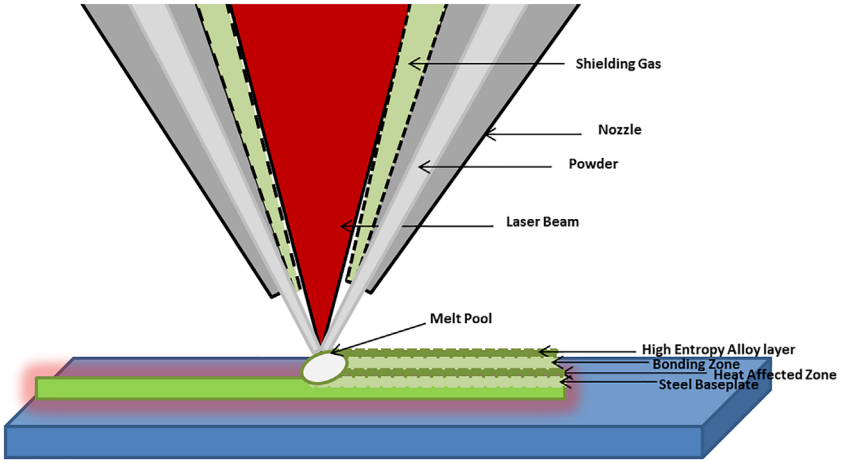

FIGURE 1 Schematic of the laser process

pool and the coating powder, the powder feeder was switched on for 5 seconds before the deposition starts. The coatings were synthesized by keeping the beam diameter and powder feed rate constant at 2 mm and 2 rpm respectively while the laser power and scanning speed varied from 600 to 1600 W at 4-12 mm/s each with a 50% overlap and layer thickness of 0.5 mm. The samples were prepared at a preheat temperature of 400°C.

After coating, the samples were sectioned into smaller pieces with a cutting blade machine and the cross-sections of the sample were prepared using standard metallographic procedures namely mounting, grinding (grit sizes 80, 320, and 1200), polishing (Tripoli, intermediates and finishing rouge) and etching with aqua regia.

2.4 | Characterization techniques

The characterizations of the samples were achieved using an Olympus $BX_{51}M$ light optical microscope (OM), XPERT-PRO X-ray diffraction system (XRD), JEOL-JSM-6010/LA Plus Scanning electron microscope (SEM) equipped with an Energy Dispersive Spectrometer (EDS).

The microhardness properties of the alloys were measured across the maximum thickness of the coatings using Matsuzawa Seiki MMT-X series Vickers hardness tester under 200 g load and 10 seconds loading time conditions.

3 | RESULTS AND DISCUSSION

3.1 | Powder analysis

Figures 2 and 3 show the powder SEM/EDS analysis using a JEOL-JSM-6010/LA plus SEM. The powders were generally smooth in texture with no agglomeration and they had particle sizes from about 45 to 106 µm, which resulted in good

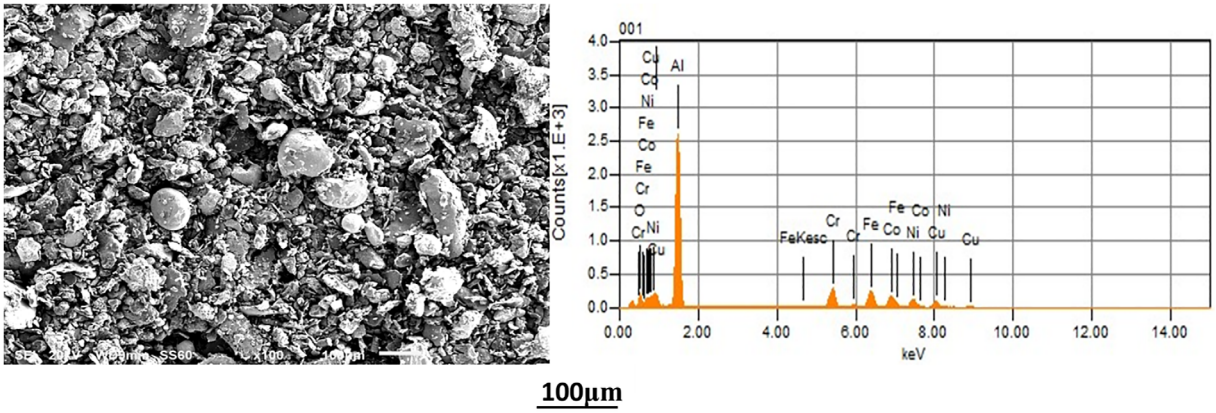

FIGURE 2 Powder morphology of AlCoCrFeNiCu HEA

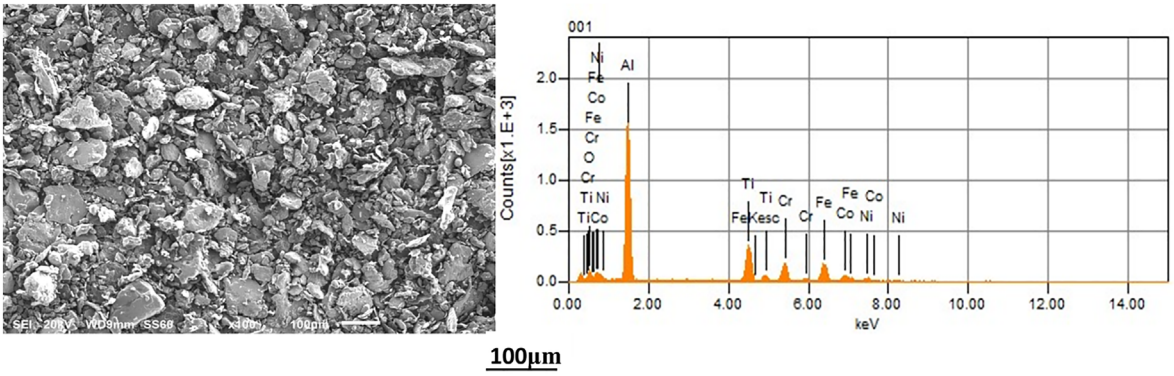

FIGURE 3 Powder morphology of AlTiCrFeCoNi HEA

flowability during deposition. There were different morphologies observed; flake irregular shapes were Cr, Fe, and Ti particles while rounded or fairly spherical shapes were Al, Cu, Ni, and Co particles.[49,50] A gray and white two-phase contrast in the powder particles of both alloys were observed, which was also reported by Mohanty, et al.[51] The white contrast corresponds with the Al, Co, Fe, Ni with a low concentration of Cr and the gray contrast corresponds with the Ti and Cu contents. The average particle size of 54 µm for AlTiCrFeCoNi HEA and 45 µm for AlCoCrFeNiCu HEA.[51,52]

According to Cantor et al,[53] the general name of elements mixed in equal or near-equal proportions should be called multicomponent alloys. However, if an alloy composition has high configurational entropy and forms solid solutions, it should be called HEAs. Furthermore, according to Boltzmann's theory, thermodynamically these alloys are HEAs because each alloy contains six principal elements with a high configurational entropy of 1.79R derived from Equation (3); this high mixing entropy lowers the Gibbs free energy of the amalgams resulting in the formation solid solutions and finally, each element has an atomic concentration between 5% and 35% which validates cantor's definition of HEAs.

$$\Delta S_{\text{mix}} = -kIn_{\text{w}} = RIn\frac{1}{n}\ RIn_{(\text{n})} \tag{3}$$

where w denotes the number of possible ways of mixes, R denotes the gas constant at 8.314 J/K mol, n denotes the number of elements in the composition, and k denotes the Boltzmann's constant.

Elemental composition observations of the EDS analysis of Al, Co, Cr, Fe, Ni, and Cu powders in Figure 2 and Al, To, Cr, Fe, Co, Ni powders in Figure 3 correspond with what was supplied by F.J Brodmann & CO., L.L.C, USA with the difference of Cu and Ti in the first and second alloy respectively.

3.2 | Effect of preheating temperature

There are various methods used in optimizing parameters such as; solidification or thermos-mechanical control and heat treatment.[54] The laser additive technique aside from its numerous advantages is also known to cause defects due to internal stresses depending on the phase transformations, cooling and solidification rate, thermal expansion coefficients, and so on. To minimize the defects observed on all samples after the first phase of experiments, preheating the base plates at 400°C was done before deposition. Preheating drives moisture and contaminants, reducing the rate at which the part cools down, thus preventing locked-in stresses which can inhibit crack formation.[55] Given this, samples without preheating temperature showed extensive cracks compared to those with preheat temperature also reported by Zhang, et al[56] and nine samples which were completely crack-free were obtained from those specimens with 400°C preheat temperature.[57] The optimal range of scanning speed and laser power for excellent dilution rates which were obtained from the crack-free samples are 8-12 mm/s, 1200-1600 W at 400°C preheating temperature, shown in Figures 4 and 5.

The solidification cracks were observed in some samples at a high scan speed and low power input, and at a low scan speed with high laser power. Previous studies have shown the effect of laser scan speed on the microstructure of laser-deposited samples.[58,59] The microstructure is determined by the solidification conditions; therefore, decreasing the velocity at an increased laser power reduces the cooling rates as shown by Equation (4) and the thermal gradient Equation (5), thus transitioning from melting to solidification.

FIGURE 4 Crack-free samples of AlCoCrFeNiCu and AlTiCrFeCoNi HEAs with optimized parameters of 1200-1600 W and 8-12 mm/s after preheating temperature

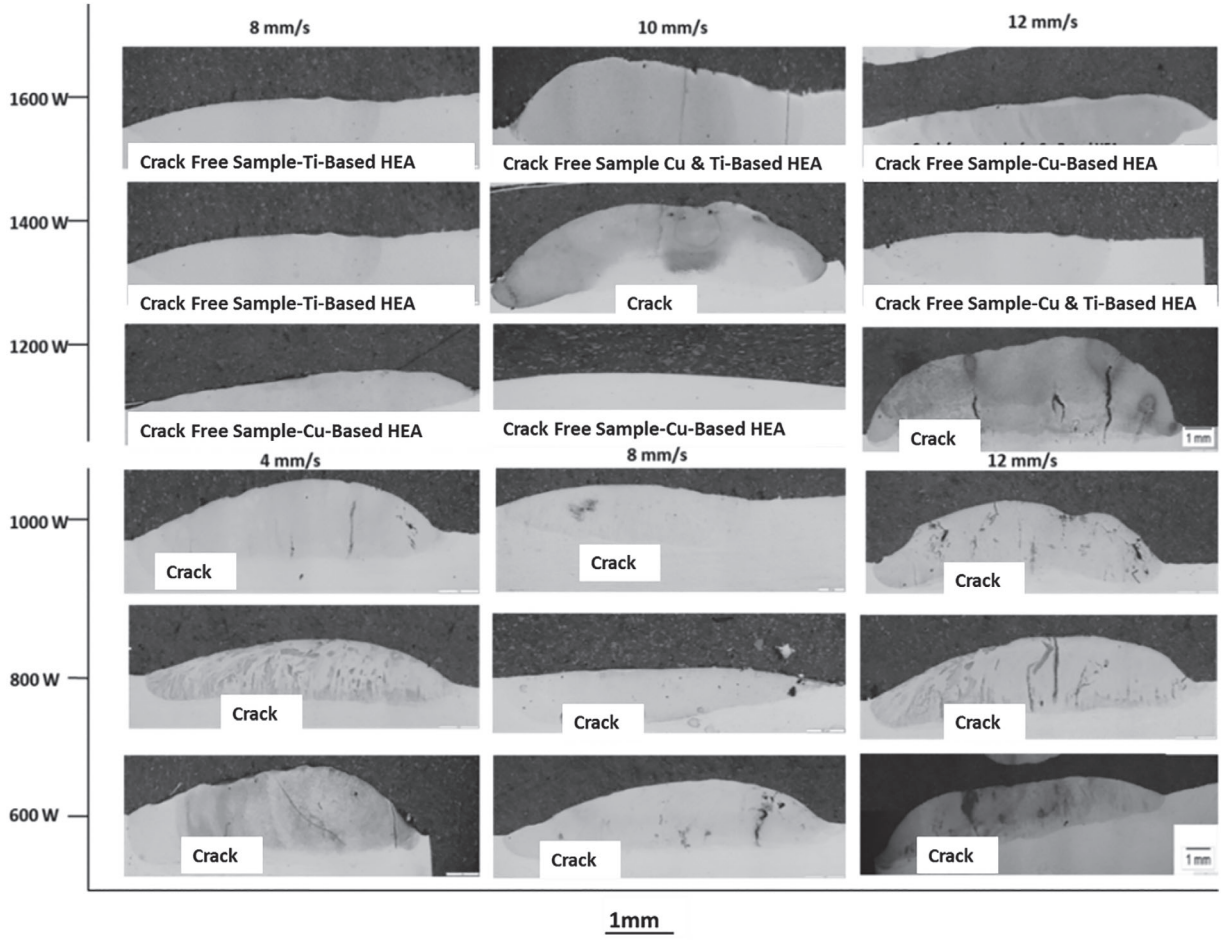

FIGURE 5 D.O.E plot showing the effect of laser parameters on the microstructure of AlCoCrFeNiCu and AlTiCrFeCoNi HEAs after stage 1 and 2 of experiments

$$\frac{dT}{dt} = \frac{-2\pi k v((T_1 - T_0)^2}{p} \tag{4}$$

$$G = \frac{dT}{dr} = \frac{-2\pi k((T_1 - T_0)^2}{Q} \tag{5}$$

Cracking occurs because of thermal stress, thus preheating reduces the stresses. The cooling rate increases proportional to the laser scan speed and it decreases with the increase in laser power. Equation (5) links the temperature gradient to the baseplate T_0 and the laser power Q, hence, an increase in the baseplate temperature, reduces the cooling rate and the thermal stresses. The increment in scan speed during dendrite formation prevented the flow of liquid, which became crack initiation sites and is influenced by stresses during solidification.[60] Thus, the cracks observed at a low scan speed,

high laser power and energy density are attributed to thermal shrinkage during deposition. At a low scan speed, the alloy powder becomes fully molten and shrinkage occurs rapidly and generating residual stresses that result in microcracks.[61] Therefore, to reduce the stresses, the preheat temperature of the baseplate was applied from room temperature to 400°C and held at 400°C. This preheat temperature reduced the cooling rates and ultimately the residual stresses. Nonetheless, the samples with optimum scan speed and laser power had the best dilution rates and defect-free structures at 1200-1600 W, 8-12 mm/s and preheating temperature of 400°C in both alloys. At a high scan speed, fast cooling occurs during solidification of the molten alloy. Nucleation and grain growth also occurs during solidification. Therefore, when the rapid solidification occurred, aggregates of the alloys within the melt pool had insufficient time for the grains to grow, resulting in the development of finer grain sizes.[62,63]

3.3 | Effect of laser parameters on the phase and microstructural analysis

3.3.1 | The phase analysis

The analysis of the X-ray diffraction patterns of AlCoCrFeNiCu and AlTiCrFeCoNi HEAs using a XPERT-PRO XRD are shown in Figures 6 and 7 at laser powers of 800 W and 1200 W and varying scanning speeds. The analysis shows a solid solution of BCC and FCC structures due to the elemental compositions of both alloys. Typical diffraction peaks associated with Al-FCC, Co-HCP (hexagonal closed-packed), Cr-BCC, Fe-BCC, Ni-FCC, and Cu-FCC for the AlCoCrFeNiCu HEA,

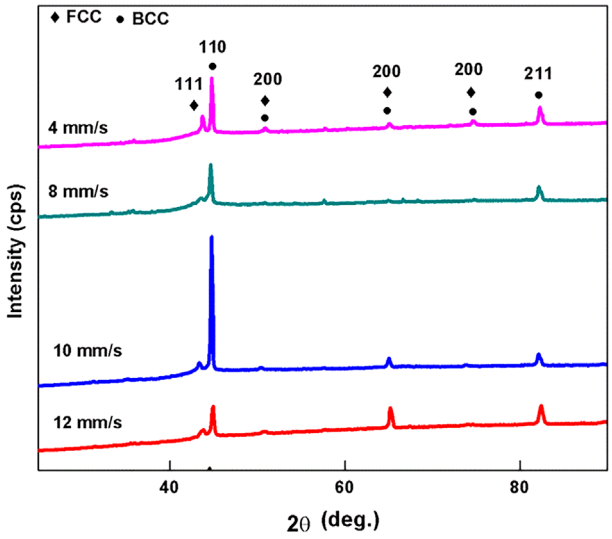

FIGURE 6 X-ray diffractograms of showing the influence of the scanning speed on the phase analysis of the in AlCoCrFeNiCu HEA

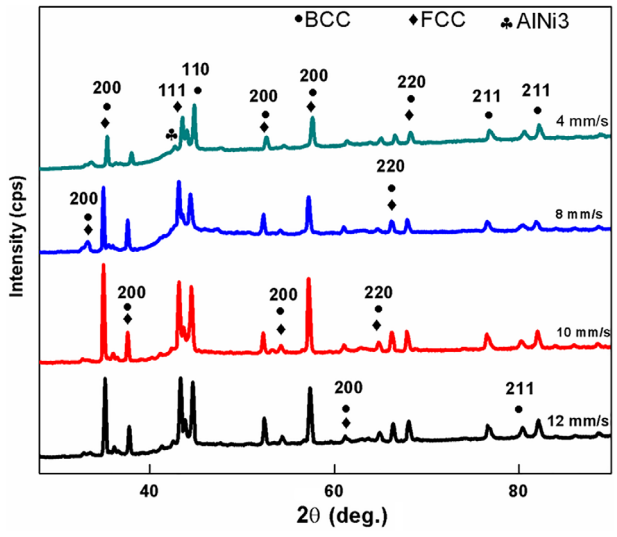

FIGURE 7 X-ray diffractograms of showing the influence of the scanning speed on the phase analysis of the AlTiCrFeCoNi HEA

and Al-FCC, Co-HCP, Cr-BCC, Fe-BCC, Ni-FCC, and Ti- HCP for AlTiCrFeCoNi HEA were identified in the results.[64,65] It was observed, with the origin Pro 8 software, that there were significant effects on the laser parameters on the phase structures of the alloys as the positions of the peaks of each sample were relatively close when compared on the same scale despite the variations in parameter.[66,67] The changes in compositions of both alloys, that is; Cu in the first alloy and Ti in the second alloy showed a different amount of phases in each alloy, respectively. There were more BCC and FCC peaks seen in both alloys attributed to the elements having lower melting points like Al with tendencies to form BCC phases, dissolving in the matrix of the composition also reported by Moravcik et al.[68-70] More so, despite the elemental effect of Cobalt and Nickel forming the FCC phase and Copper segregating to the interdendritic region to form a Cu-rich FCC phase, the AlCoCrFeNiCu HEA was still more of a BCC solid solution structure.[71,72] The AlTiCrFeCoNi HEA compared to the AlCoCrFeNiCu HEA had more peaks suggesting either an excessive grain refinement induced by the rapid solidification process or the lattice distortion effect.[68,73]

For the AlCoCrFeNiCu HEA, the highest peak at 45° showed the BCC phases and most peaks observed were mostly BCC, however, the FCC peak was more prominent at a scan speed of 4 mm/s. This significant peak occurrence is attributed to deposition process where higher scanning speeds leads to higher cooling rates and the high rate of cooling during deposition inhibits the formation of the FCC phase.[74,75] This FCC peak also confirms the segregation of Cu to the inter dendrites as the peak consists mostly of Cu.[76,77] The AlCoCrFeNiCu HEA in Figure 6 has its most dominant diffraction peak at $2\theta = 44.5°$ and AlTiCrFeCoNi HEA in Figure 7 was at 35.174°. These phases consist of Iron-Nickel and Aluminum Nickel respectively with solid solubility at 912°C according to TCFE6 thermodynamic database and Thermo Calc.[78] There were no notable changes in the XRD patterns with changes in laser power for the Cu-based HEA yet, at a change in scanning speed, significant changes were observed.[79-81] The BCC peaks were more prominent as the scanning speed increases and the FCC peak showed its angle intensity at lower scan speeds which suggest that the alloy has a higher volume fraction of the BCC phase and this may be attributed to the high cooling rates during LAM which occurs as the scanning speed increases which has been reported to be a good influence in inhibiting the formation of FCC phase structure. Cui et al[75] fabricated AlCoCrFeNi HEA via laser deposition on an AISI 304 substrate and the authors also reported the inhibition of FCC structure formation due to the high cooling rates of the deposition process.[74,82]

The intermetallic $AlNi_3$ phase ($L1_2$, FCC) is said to be responsible for an increase in the mechanical properties of the AlTiCrFeCoNi alloy.[83] The large Al content in AlCoCrFeNiCu and Al/Ti content in AlTiCrFeCoNi favored the formation of more BCC phases over FCC phase and is attributed to the large atomic size of the elements.[84] The BCC structure is known to have lower atomic packing density than the FCC resulting in the accommodation of larger solute atoms.[85,86] The gradual change in lattice parameters means fewer weak phases exist within the layers. The XRD spectrum of the AlTiCrFeCoNi HEA in Figure 7 shows the highest peak consisting of BCC (Cr-Fe) (Fe-Ti) phases with no significant changes with change in parameters. Titanium is observed to have an impact on the composition of the phases due to its large atomic radius difference in contrast to other elements while favoring the formation of more BCC phases over FCC phase.[87] The high entropy effect is responsible for the decrease in Gibbs free energy stabilizing the solid solution in the alloy system.[88,89]

3.3.2 | The microstructural analysis

Figure 8 shows the photomicrograph of the cross-section of the HEAs perpendicular to the build direction and investigated using an Olympus BX51M light Optical Microscope. The laser energy density was beneficial in the removal of defects. A decrease in the scan velocity and increase in laser power increased the energy density. It was observed that after preheating the baseplate, optimized laser parameters between 1200-1600 W and 8-12 mm/s, all had their energy densities exceeding 50 J/mm^2. Therefore, it can be deduced that high energy densities are beneficial in the elimination of defects. The parameters showed homogeneously formed microstructures in the clad zones with good dilution zones at their respective interfaces and adhesion between the baseplates and the clad without defects as shown in Figure 8.

The advantage of the laser deposition technique has over conventional methods is the rapid solidification rate.[90] The dendritic structures observed in Figure 9 are due to the solidification rates during deposition of the HEAs. The image provides a view of the microstructural contrast between the two HEAs; AlCoCrFeNiCu HEA showed columnar dendritic structure while AlTiCrFeCoNi HEA showed an equiaxed dendritic structure. Columnar dendritic structures are reported to have a strong preference for growing over one direction, which is almost at right angles with the interface. The AlCoCrFeNiCu HEA columnar grains were formed under very constrained growth along the direction of the positive thermal gradient.[91] The growth direction of the grains was influenced by the surface energy, the rate of solidification and the

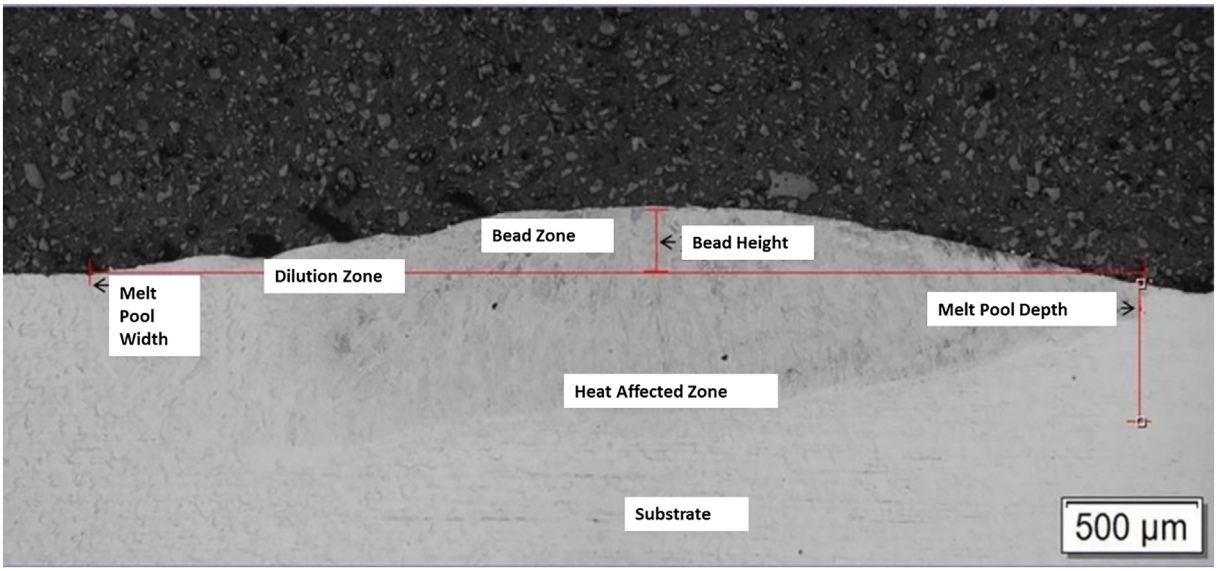

FIGURE 8 Subsection of the high entropy alloy geometry

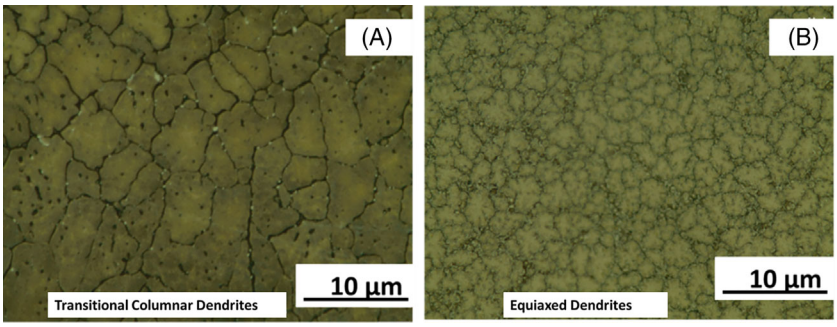

FIGURE 9 The optical micrograph patterns (A) AlCoCrFeNiCu (B) AlTiCrFeCoNi HEA

growth kinetics. Thus, the grain growth direction resulted in a reduction of the number of grains with orientation facing the same direction.[92,93]

According to Equation (6), the ASTM grain size number measurements for AlCoCrFeNiCu and AlTiCrFeCoNi HEAs per square inch and at a Magnification of 10× was approximately 4.91 and 5.25 respectively.

$$N = 2^{n-1} \tag{6}$$

Where N denotes the number of grains per square inch at a magnification of 100× and n denotes the grain size number.

Fine equiaxed grains observed in AlTiCrFeCoNi HEA are known to help limit solidification cracking and improve its mechanical properties. This is attributed to the presence of the low melting point segregates with high negative mixing enthalpy consisting of Ni and Al that are distributed over a large grain boundary area; and these grains allow more transport of liquid between the grains.[94,95] The equiaxed dendritic structure is characterized by a growth structure with similar sizes in all directions of the melt.[96,97] The interface during solidification grows in the direction where the temperature gradient is at its maximum. The interface growth rate is associated with the laser velocity, thus, the increase or decrease in solidification rates is influenced by the growth rate (R), scanning velocity and the temperature gradient (G). Therefore, the relationship between the scanning speed (mm/s) and the dendritic growth rate (R) is expressed in Equation (7).[98]

$$R = \frac{V \cos \alpha}{\cos(\alpha - \beta)} \tag{7}$$

where α denotes the angle between the direction perpendicular to the molten pool and the direction of the clad, β denotes the angle between the growth direction of the dendritic structure.[99] At the interface, a minimum R and a maximum G

will lead to a larger G/R value. Hence, from the interface to the clad surface the ratio of the G/R decreases and this often makes a dendritic structure.[90,100] The columnar dendritic structure of the AlCoCrFeNiCu HEA had a typical dendrite and interdendrite structure and the interdendritic region showed that it consists mostly of Cu.[101] The segregation of Cu to the inter dendrite is expected as obtained in the literature. This is attributed to the low binding energy of Cu with other elements like Co, Fe, Ni, and Cr, yet, it has a high mixing enthalpy with these elements. Thus, during rapid solidification, copper is displaced and segregates to the interdendritic region.[102,103]

The high Al content in both alloys caused spinodal decomposition, which is prevalent in most HEAs containing aluminum.[52] The Al content above 11.0 at% produces redundant aluminum atoms, which form BCC phases with a spinodal structure that matches those reported by Wang et al.[104] Al is known to have the FCC structure nonetheless, it is also known to contribute to the stabilization of the BCC phase.[65] Aluminum and Nickel in the AlTiCrFeCoNi with low melting points may have entered into the melt pool first through the laser beam, allowing the elements to have enough contact time to form the $AlNi_3$ phase.

3.4 | Effect of laser parameters on hardness

The surface plots in Figures 10 and 11 were extracted from Stat-Ease Design-Expert Software 11 and they show a three-dimensional representation of the functional relationship between the laser parameters and the microhardness of the HEAs. A Matsuzawa Seiki MMT-X series Vickers hardness tester under 200 g load and 10 seconds loading time conditions were used to experimentally investigate the microhardness properties of the HEAs as shown in Figure 12A,B.

The mechanical strength of HEAs in the as-deposited states is greatly dependent on the solidification microstructure.[105] According to the Hall-Petch grain boundary strengthening relation, the equation where σ is the Stephan-Boltzmann constant plus the factor K, times the inverse of the square root of the grain size D, demonstrates that hardness is greatly improved by grain size reduction in laser deposition, which is as a result of fast cooling given by Equation (8).[106]

$$\sigma_{0=}\sigma_i + {}^{k}/\sqrt{D} \tag{8}$$

Generally, there was an increase in the hardness properties of the HEAs from 389 to 837 HV for the AlCoCrFeNiCu HEA and 380-521 HV as the laser power increases from 1200 W to 1600 W and 1200 W to 1400 W respectively. Therefore, the laser power had the most significant influence on the mechanical property of the alloys, which is in agreement with the microstructure. Thus, it is recommended that increasing laser power which increases the energy density can yield defect-free microstructures and enhanced mechanical properties.

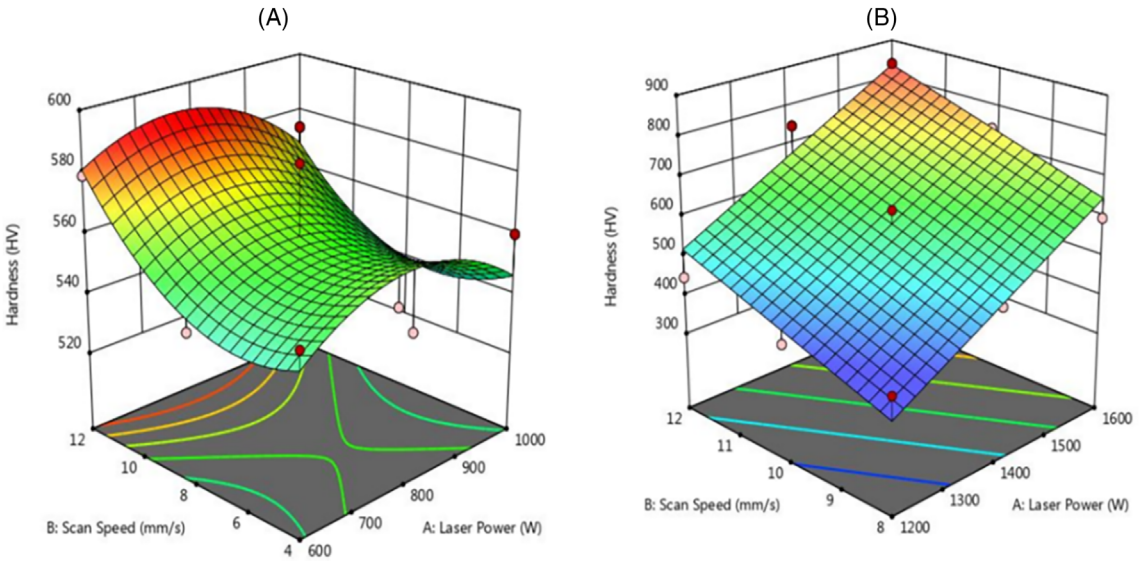

FIGURE 10 D.O.E surface plot showing the effect of laser parameters on the microhardness of AlCoCrFeNiCu HEA (A) stage 1 of experiments (B) stage 2 of experiments

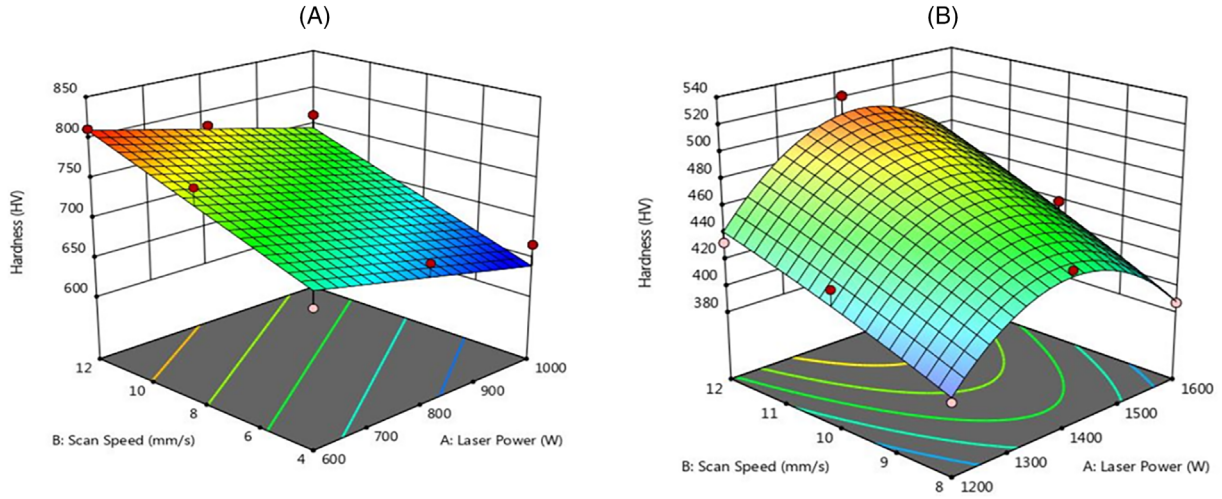

FIGURE 11 D.O.E surface plot showing the effect of laser parameters on the microhardness of AlTiCrFeCoNi HEA (A) stage 1 of experiments (B) stage 2 of experiments

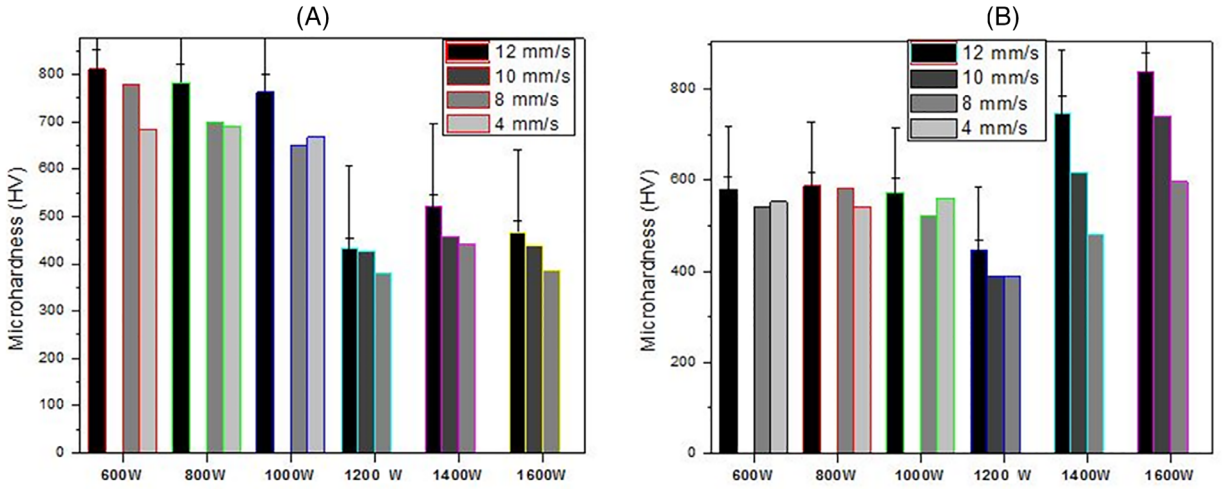

FIGURE 12 Microhardness chart showing stage 1 and stage 2 of experiments (A) AlTiCrFeCoNi HEA (B) AlCoCrFeNiCu HEA

The increase in the hardness properties of the amalgams can also be attributed to the grain boundary strengthening due to the significant BCC phases observed.[107] This indicates that the BCC phase is stronger than the FCC phase because in the packing planes {110} of the BCC structure, a slip along this plane is more difficult than the FCC {111} plane. Furthermore, the denser and regular {111} plane contains lower lattice friction for dislocation motion and greater interplanar spacing compared to the {110} plane, thus giving the BCC structure excellent solution hardening mechanism.[108] On the other hand, there were variations with sharp changes in the microhardness values of AlTiCrFeCoNi HEA at stage one of the experiments, which could be attributed to the small hardening effect in the heat-affected zones and the inner microstructure undergoing intricate phenomena before preheating under reoccurring thermal cycling resulting in the fluctuation in hardness values.[109]

Consequently, the AlTiCrFeCoNi alloy's had higher hardness values at the first stage of experiments from 600 W to 1000 W attributed to the $AlNi_3$ phase and the BCC structure.[110] Nonetheless, there was a decline at the second stage of experiments from 1200 W to 1600 W with an average hardness ranging from 811 to 387 HV compared to AlCoCrFeNiCu HEA, which ranged from 389 to 837 HV after stage one and two of the experiments. Even so, both alloys showed the good hardness values attributed to the optimized process parameters, the BCC solid solution phase and the rapid solidification of the LAM process compared with other conventional methods.[111]

4 | CONCLUSION

LAM was used to synthesize AlCoCrFeNiCu and AlTiCrFeCoNi HEAs on a steel baseplate, and the effect of laser parameters on both compositions was studied. The laser power was varied between 600 and 1600 W with the laser scan speed varied from 4 to 12 mm/s while the powder feed rate and the gas flow rates were kept constant at 2 rpm and 3 l/min, respectively. The study deduced that:

- Optimizing the laser parameters invariably influenced the performance of the alloys positively with potential coatings and structural applications.
- The alloys both showed a dendritic structure with FCC and BCC phases.
- The optimized parameters were between 1200 and 1600 W at 8-12 mm/s with a 50% overlap. This shows that the right combination of process parameters is an important factor in producing homogeneous and defect-free microstructures.
- The AlCoCrFeNiCu HEA showed fewer peaks on the XRD graph and had few FCC phases compared to the AlTiCrFeCoNi HEA. This is attributed to the difference in Cu and Ti contents, respectively.
- After the first stage of experiments, the AlTiCrFeCoNi HEA had higher hardness values than the AlCoCrFeNiCu HEA; however, at the second stage, the AlCoCrFeNiCu HEA showed high hardness than the AlTiCrFeCoNi HEA. This is attributed to the changes in process parameters and the introduction of the preheating temperature at the second stage.
- Both alloys showed an increase in hardness values at a scan speed of 12 mm/s. This may be attributed to the rapid solidification of the deposition process which occurs at a high scan speed, and this leads to grain refinement and enhances the properties of the alloys.

ACKNOWLEDGEMENTS

The authors would like to appreciate the Council for Scientific and Research (CSIR), the National Laser Center (Laser Enabled Manufacturing Resource Group), Mr Samuel Skhosane and the Tshwane University of Technology, Pretoria, South Africa for their technical and scientific support during this research.

PEER REVIEW INFORMATION

Engineering Reports thanks Li Jiang, Prashanth Konda Gokuldoss, Vladimir V. Popov Jr., and other anonymous reviewer(s) for their contribution to the peer review of this work.

PEER REVIEW

The peer review history for this article is available at https://publons.com/publon/10.1002/eng2.12252.

AUTHORS CONTRIBUTION

Modupeola Dada contributed to the conceptualization, data curation, formal analysis, investigation, methodology, writing the original draft. Patricia Popoola contributed to the project administration, resources, supervision, writing the review and editing. Ntombi Mathe contributed to the project administration, resources, supervision, writing the review and editing. Sisa Pityana contributed to the project administration, resources, software, writing the review and editing. Samson Adeosun contributed to the project administration, supervision, writing the review and editing. Olufemi Aramide contributed to the supervision, writing the review and editing. Thabo Lengopeng contributed to the investigation, writing the review and editing.

CONFLICT OF INTEREST

The authors declare that there is no potential conflict of interest.

ORCID

Modupeola Dada https://orcid.org/0000-0002-9227-197X

REFERENCES

1. Singh R. *Introduction to Basic Manufacturing Processes and Workshop Technology*. India: New Age International Pvt. Ltd; 2006:2006.
2. Gibson I, Rosen DW, Stucker B. *Additive Manufacturing Technologies*. Vol 17. New York: Springer; 2014.
3. A. Gebhardt and J. Hötter, Additive manufacturing: 3D printing for prototyping and manufacturing, *Additive Manufacturing*: Hanser, pp. 93–290, 2016.

4. DebRoy T, Wei H, Zuback J, et al. Additive manufacturing of metallic components – process, structure and properties. *Prog Mater Sci*. 2018;92:112-224.
5. ASTM I. *ASTM52900-15 Standard Terminology for Additive Manufacturing—General Principles—Terminology*. West Conshohocken, PA: ASTM International; 2015.
6. Harun W, Kamariah M, Muhamad N, Ghani S, Ahmad F, Mohamed Z. A review of powder additive manufacturing processes for metallic biomaterials. *Powder Technol*. 2018;2017.128–151.
7. Gorsse S, Hutchinson C, Gouné M, Banerjee R. Additive manufacturing of metals: a brief review of the characteristic microstructures and properties of steels, Ti-6Al-4V and high-entropy alloys. *Sci Technol Adv Mater*. 2017;18:584-610.
8. Uhlmann E, Kersting R, Klein TB, Cruz MF, Borille AV. Additive manufacturing of titanium alloy for aircraft components. *Procedia Cirp*. 2015;35:55-60.
9. T. Wohlers. *Wohler's Report 2013*. Belgium: Leuven University Press; 2013.
10. Waterman NA, Dickens P. Rapid product development in the USA, Europe and Japan. *World Class Des Manuf*. 1994;1:27-36.
11. Guo N, Leu M. Additive manufacturing: technology, applications and research needs. *Front Mech Eng*. 2013;8(3):215-243.
12. Dilip J, Zhang S, Teng C, et al. Influence of processing parameters on the evolution of melt pool, porosity, and microstructures in Ti-6Al-4V alloy parts fabricated by selective laser melting. *Prog Addit Manuf*. 2017;2:157-167.
13. Brückner F, Lepski D, Beyer E. Modeling the influence of process parameters and additional heat sources on residual stresses in laser cladding. *J Ttherm Spray Technol*. 2007;16:355-373.
14. Wang L, Felicelli S, Gooroochurn Y, Wang P, Horstemeyer M. Optimization of the LENS® process for steady molten pool size. *Mater Sci Eng A*. 2008;474:148-156.
15. Dass A, Moridi A. State of the art in directed energy deposition: from additive manufacturing to materials design. *Coatings*. 2019;9:418.
16. Gibson I, Rosen DW, Stucker B. Additive manufacturing technologies. *Google Scholar*. New York: Springer; 2010.
17. Al-Khazraji KK, Majed RA, Abdulhameed ZN. Effect of uric acid level on the corrosion behavior of SS 316L and co-Cr-Mo used in implant applications. *Eng Technol J*. 2013;31:3382-3390.
18. Loicq R. *Additive Manufacturing Utilized for Prototype Parts*. Finland: TAMK publications; 2017.
19. Gu D. *Laser Additive Manufacturing of High-Performance Materials*. Germany: Springer-Verlag; 2015.
20. Griffith ML, Ensz MT, Puskar JD, et al. Understanding the microstructure and properties of components fabricated by laser engineered net shaping (LENS). *MRS Online Proc Libr Arch*. 2000;625.
21. Aghasibeig M, Fredriksson H. Laser cladding of a featureless iron-based alloy. *Surf Coat Technol*. 2012;209:32-37.
22. M. Dada, P. Popoola, S. Adeosun, and N. Mathe, High entropy alloys for aerospace applications, *Environmental Impact of Aviation and Sustainable Solutions*. London: IntechOpen; 2019.
23. Svensson DO. High Entropy Alloys: Breakthrough Materials for Aero Engine Applications? [master's thesis]. Sweden: Chalmers University of Technology; 2014.
24. Chikumba S, Rao VV. High entropy alloys: development and applications. Paper presented at: 7th Int. Conf. Latest Trends Eng. Technol; 2015:1-5.
25. Gao MC, Yeh J-W, Liaw PK, Zhang Y. *High-Entropy Alloys*. Switzerland: Springer International Publishing; 2016.
26. Yeh JW, Chen SK, Lin SJ, et al. Nanostructured high-entropy alloys with multiple principal elements: novel alloy design concepts and outcomes. *Adv Eng Mater*. 2004;6:299-303.
27. Murty BS, Yeh J-W, Ranganathan S. *High-entropy Alloys*. United Kingdom: Butterworth-Heinemann, Elsevier; 2014.
28. Shafeie S, Guo S, Hu Q, Fahlquist H, Erhart P, Palmqvist A. High-entropy alloys as high-temperature thermoelectric materials. *J Appl Phys*. 2015;118:184905.
29. Tong C-J, Chen Y-L, Yeh J-W, et al. Microstructure characterization of Al x CoCrCuFeNi high-entropy alloy system with multiprincipal elements. *Metal Mater Trans A*. 2005;36:881-893.
30. Kao Y-F, Chen T-J, Chen S-K, Yeh J-W. Microstructure and mechanical property of as-cast,-homogenized, and-deformed AlxCoCrFeNi ($0 \leq x \leq 2$) high-entropy alloys. *J Alloys Compd*. 2009;488:57-64.
31. Hemphill MA, Yuan T, Wang G, et al. Fatigue behavior of Al0. 5CoCrCuFeNi high entropy alloys. *Acta Mater*. 2012;60:5723-5734.
32. Zhou R, Liu Y, Zhou C, et al. Microstructures and mechanical properties of C-containing FeCoCrNi high-entropy alloy fabricated by selective laser melting. *Intermetallics*. 2018;94:165-171.
33. Jiang H, Han K, Li D, Cao Z. Synthesis and characterization of AlCoCrFeNiNbx high-entropy alloy coatings by laser cladding. *Crystals*. 2019;9:56.
34. Zhu Z, Nguyen Q, Ng F, et al. Hierarchical microstructure and strengthening mechanisms of a CoCrFeNiMn high entropy alloy additively manufactured by selective laser melting. *Scr Mater*. 2018;154:20-24.
35. Popov VV, Katz-Demyanetz A, Koptyug A, Bamberger M. Selective electron beam melting of Al0. 5CrMoNbTa0. 5 high entropy alloys using elemental powder blend. *Heliyon*. 2019;5:e01188.
36. Chao Q, Guo T, Jarvis T, Wu X, Hodgson P, Fabijanic D. Direct laser deposition cladding of AlxCoCrFeNi high entropy alloys on a high-temperature stainless steel. *Surf Coat Technol*. 2017;332:440-451.
37. Mahamood RM, Akinlabi ET. Modelling and optimization of laser additive manufacturing process of Ti alloy composite. *Optimization of Manufacturing Processes*. United States: Springer Cham; 2020:91-109.
38. Aboutaleb AM, Bian L, Elwany A, Shamsaei N, Thompson SM, Tapia G. Accelerated process optimization for laser-based additive manufacturing by leveraging similar prior studies. *IISE Trans*. 2017;49:31-44.
39. Baturynska I, Semeniuta O, Martinsen K. Optimization of process parameters for powder bed fusion additive manufacturing by combination of machine learning and finite element method: A conceptual framework; 2018.

40. Hofman JT. *Development of an Observation and Control System for Industrial Laser Cladding*. University of Twente, Enschede Netherlands; 2009.
41. Steen WM, Mazumder J. *Laser Material Processing*. Germany: Springer Science & Business Media; 2010.
42. Prashanth K, Scudino S, Maity T, Das J, Eckert J. Is the energy density a reliable parameter for materials synthesis by selective laser melting? *Mate Res Lett*. 2017;5:386-390.
43. Olakanmi E, Sepako M, Morake J, Hoosain SE, Pityana SL. Microstructural characteristics, crack frequency and diffusion kinetics of functionally graded Ti-Al composite coatings: effects of laser energy density (LED). *JOM*. 2019;71:900-911.
44. Zuback J, DebRoy T. The hardness of additively manufactured alloys. *Materials*. 2018;11:2070.
45. Ermurat M, Ali Arslan M, Erzincanli F, Uzman I. Process parameters investigation of a laser-generated single clad for minimum size using design of experiments. *Rapid Prototyp J*. 2013;19:452-462.
46. Graf B, Ammer S, Gumenyuk A, Rethmeier M. Design of experiments for laser metal deposition in maintenance, repair and overhaul applications. *Procedia CIRP*. 2013;11:245-248.
47. Liao H-T, Shie J-R. Optimization on selective laser sintering of metallic powder via design of experiments method. *Rapid Prototyp J*. 2007;13:156-162.
48. Fatoba O, Adesina O, Farotade G, Adediran A. Modelling and optimization of laser alloyed AISI 422 stainless steel using taguchi approach and response surface model (RSM). *Curr J Appl Sci Technol*. 2017;23:1-16.
49. Gómez-Esparza CD, Baldenebro-López F, González-Rodelas L, Baldenebro-López J, Martínez-Sánchez R. Series of nanocrystalline NiCoAlFe (Cr, cu, Mo, Ti) high-entropy alloys produced by mechanical alloying. *Mater Res*. 2016;19:39-46.
50. Löbel M, Lindner T, Kohrt C, Lampke T. Processing of AlCoCrFeNiTi high entropy alloy by atmospheric plasma spraying. Paper presented at: IOP Conference Series: Materials Science and Engineering; 2017:012015.
51. Mohanty S, Maity T, Mukhopadhyay S, et al. Powder metallurgical processing of equiatomic AlCoCrFeNi high entropy alloy: microstructure and mechanical properties. *Mater Sci Eng A*. 2017;679:299-313.
52. Zhang Y, Zuo TT, Tang Z, et al. Microstructures and properties of high-entropy alloys. *Prog Mater Sci*. 2014;61:1-93.
53. Cantor B, Chang I, Knight P, Vincent A. Microstructural development in equiatomic multicomponent alloys. *Mater Sci Eng A*. 2004;375:213-218.
54. Li J, Jia W, Wang J, Kou H, Zhang D, Beaugnon E. Enhanced mechanical properties of a CoCrFeNi high entropy alloy by supercooling method. *Mater Des*. 2016;95:183-187.
55. Khaled T. Preheating, interpass and post-weld heat treatment requirements for welding low alloy steels. 2014;6:1-14.
56. Zhang H, Shi Y, Kutsuna M, Xu G. Laser cladding of Colmonoy 6 powder on AISI316L austenitic stainless steel. *Nucl Eng Des*. 2010;240:2691-2696.
57. Dada M, Popoola P, Mathe N, Pityana S, Adeosun S, Lengopeng T. Fabrication and hardness behaviour of high entropy alloys. Paper presented at: *TMS* 2020 149th Annual Meeting & Exhibition Supplemental Proceedings; 2020:1581-1591.
58. Akinlabi ET, Mahamood RM, Shukla M, Pityana S. *Effect of Scanning Speed on Material Efficiency of Laser Metal Deposited Ti6Al4V*. Paris: World Academy of Science and Technology; 2012.
59. Wang X, Gong X, Chou K. Scanning speed effect on mechanical properties of Ti-6Al-4V alloy processed by electron beam additive manufacturing. *Procedia Manuf*. 2015;1:287-295.
60. Coniglio N, Cross CE. Mechanisms for solidification crack initiation and growth in aluminum welding. *Metal Mater Trans A*. 2009;40:2718-2728.
61. Hofmeister W, Griffith M. Solidification in direct metal deposition by LENS processing. *JOM*. 2001;53:30-34.
62. Thijs L, Verhaeghe F, Craeghs T, Van Humbeeck J, Kruth J-P. A study of the microstructural evolution during selective laser melting of Ti–6Al–4V. *Acta Mater*. 2010;58:3303-3312.
63. Farotade GA, Popoola AP. A study on microhardness and microstructural evolution of titanium/zirconium diboride cermet coatings with varying scan speeds during laser cladding on Ti6Al4V substrate. *Int J Microstruct Mater Prop*. 2017;12:25-37.
64. Wang Y, Ma S, Chen X, Shi J, Zhang Y, Qiao J. Optimizing mechanical properties of AlCoCrFeNiTi x high-entropy alloys by tailoring microstructures. *Acta Metal Sin*. 2013;26:277-284.
65. Tung C-C, Yeh J-W, Shun T-t, Chen S-K, Huang Y-S, Chen H-C. On the elemental effect of AlCoCrCuFeNi high-entropy alloy system. *Mater Lett*. 2007;61:1-5.
66. Tian L-H, Xiong W, Liu C, Lu S, Fu M. Microstructure and wear behavior of atmospheric plasma-sprayed AlCoCrFeNiTi high-entropy alloy coating. *J Mater Eng Perform*. 2016;25:5513-5521.
67. Wen L, Kou H, Li J, Chang H, Xue X, Zhou L. Effect of aging temperature on microstructure and properties of AlCoCrCuFeNi high-entropy alloy. *Intermetallics*. 2009;17:266-269.
68. Moravcik I, Cizek J, Gavendova P, Sheikh S, Guo S, Dlouhy I. Effect of heat treatment on microstructure and mechanical properties of spark plasma sintered AlCoCrFeNiTi0. 5 high entropy alloy. *Mater Lett*. 2016;174:53-56.
69. Chen W, Fu Z, Fang S, Xiao H, Zhu D. Alloying behavior, microstructure and mechanical properties in a FeNiCrCo0. 3Al0. 7 high entropy alloy. *Mater Des*. 2013;51:854-860.
70. Suryanarayana C. Mechanical alloying and milling. *Prog Mater Sci*. 2001;46:1-184.
71. Soare V, Mitrica D, Constantin I, et al. Influence of remelting on microstructure, hardness and corrosion behaviour of AlCoCrFeNiTi high entropy alloy. *Mater Sci Technol*. 2015;31:1194-1200.
72. Dolique V, Thomann A-L, Brault P, Tessier Y, Gillon P. Complex structure/composition relationship in thin films of AlCoCrCuFeNi high entropy alloy. *Mater Chem Phys*. 2009;117:142-147.

73. Yue T, Xie H, Lin X, Yang H, Meng G. Solidification behaviour in laser cladding of AlCoCrCuFeNi high-entropy alloy on magnesium substrates. *J Alloys Compd*. 2014;587:588-593.
74. Wang R, Zhang K, Davies C, Wu X. Evolution of microstructure, mechanical and corrosion properties of AlCoCrFeNi high-entropy alloy prepared by direct laser fabrication. *J Alloys Compd*. 2017;694:971-981.
75. Cui W, Karnati S, Zhang X, Burns E, Liou F. Fabrication of AlCoCrFeNi high-entropy alloy coating on an AISI 304 substrate via a CoFe2Ni intermediate layer. *Entropy*. 2019;21:2.
76. Gwalani B, Choudhuri D, Soni V, et al. Cu assisted stabilization and nucleation of L12 precipitates in Al0. 3CuFeCrNi2 fcc-based high entropy alloy. *Acta Mater*. 2017;129:170-182.
77. Derimow N, Clark T, Roach C, Mathaudhu S, Abbaschian R. Processing pathway effects in CoCrCuNi+ X (Fe, Mn) high-entropy alloys. *Philos Mag*. 2019;99:1-15.
78. Bratberg J. *"TCFE6–TCS Steels/Fe–Alloys Database," Version 6.2: Tech. Rep.: Thermo–Calc software AB*. Stockholm, Sweden: Thermo–Calc Software AB; 2011.
79. Li W, Liu J, Zhou Y, et al. Effect of laser scanning speed on a Ti-45Al-2Cr-5Nb alloy processed by selective laser melting: microstructure, phase and mechanical properties. *J Alloys Compd*. 2016;688:626-636.
80. Chen S, Tong Y, Liaw PK. Additive manufacturing of high-entropy alloys: a review. *Entropy*. 2018;20:937.
81. Mathe NR, Tshabalala LC. The validation of the microstructural evolution of selective laser-melted AlSi10Mg on the in-house built machine: energy density studies. *Prog Addit Manuf*. 2019;4:431-442.
82. Munitz A, Salhov S, Hayun S, Frage N. Heat treatment impacts the micro-structure and mechanical properties of AlCoCrFeNi high entropy alloy. *J Alloys Compd*. 2016;683:221-230.
83. Chen M-R, Lin S-J, Yeh J-W, Chen S-K, Huang Y-S, Tu C-P. Microstructure and properties of Al0. 5CoCrCuFeNiTix (x= 0–2.0) high-entropy alloys. *Mater Trans*. 2006;47:1395-1401.
84. Dolique V, Thomann A-L, Brault P, Tessier Y, Gillon P. Thermal stability of AlCoCrCuFeNi high entropy alloy thin films studied by in-situ XRD analysis. *Surf Coat Technol*. 2010;204:1989-1992.
85. Yeh JW, Chen YL, Lin SJ, Chen SK. High-entropy alloys–a new era of exploitation. *Materials Science Forum*. Switzerland: Trans Tech Publications Ltd; 2007:1-9.
86. Shaysultanov D, Stepanov N, Kuznetsov A, Salishchev G, Senkov O. Phase composition and superplastic behavior of a wrought AlCoCrCuFeNi high-entropy alloy. *JOM*. 2013;65:1815-1828.
87. Zhang K, Fu Z, Zhang J, et al. Microstructure and mechanical properties of CoCrFeNiTiAlx high-entropy alloys. *Mater Sci Eng A*. 2009;508:214-219.
88. Ye Y, Wang Q, Lu J, Liu C, Yang Y. High-entropy alloy: challenges and prospects. *Mater Today*. 2016;19:349-362.
89. Löbel M, Lindner T, Mehner T, Lampke T. Microstructure and wear resistance of AlCoCrFeNiTi high-entropy alloy coatings produced by HVOF. *Coatings*. 2017;7:144.
90. Jiang L, Wu W, Cao Z, Deng D, Li T. Microstructure evolution and wear behavior of the laser cladded CoFeNi 2 V 0.5 Nb 0.75 and CoFeNi 2 V 0.5 Nb high-entropy alloy coatings. *J Therm Spray Technol*. 2016;25:806-814.
91. Dubrov A, Mirzade FK, Dubrov V. On multi-scale modelling of dendrite growth during laser metal deposition process. *3D Printed Optics and Additive Photonic Manufacturing*. USA: International Society for Optics and Photonics; 2018:1067514.
92. Zaeem MA, Yin H, Felicelli SD. Modeling dendritic solidification of Al–3% cu using cellular automaton and phase-field methods. *Appl Math Model*. 2013;37:3495-3503.
93. Trivedi R, Kurz W. Dendritic growth. *Int Mater Rev*. 1994;39:49-74.
94. Zhang Y, Pan C, Male A. Improved microstructure and properties of 6061 aluminum alloy weldments using a double-sided arc welding process. *Metal Mater Trans A*. 2000;31:2537-2543.
95. Löbel M, Lindner T, Mehner T, Lampke T. Influence of titanium on microstructure, phase formation and wear behaviour of AlCoCrFeNiTix high-entropy alloy. *Entropy*. 2018;20:505.
96. Shun T-T, Hung C-H, Lee C-F. Formation of ordered/disordered nanoparticles in FCC high entropy alloys. *J Alloys Compd*. 2010;493:105-109.
97. Lindner T, Löbel M, Mehner T, Dietrich D, Lampke T. The phase composition and microstructure of AlxCoCrFeNiTi alloys for the development of high-entropy alloy systems. *Metals*. 2017;7:162.
98. Jelvani S, Razavi RS, Barekat M, Dehnavi MR, Erfanmanesh M. Evaluation of solidification and microstructure in laser cladding Inconel 718 superalloy. *Opt Laser Technol*. 2019;120:105761.
99. Sun P, Fang ZZ, Zhang Y, Xia Y. Review of the methods for production of spherical Ti and Ti alloy powder. *JOM*. 2017;69:1853-1860.
100. Lu C, Wang Y, Lei X, et al. Influence of Fe-W intermetallic compound on fracture behavior of steel/tungsten HIP diffusion bonding joint: experimental investigation and first-principles calculation. *J Manuf Process*. 2020;55:131-142.
101. Yue T, Xie H, Lin X, Yang H, Meng G. Microstructure of laser re-melted AlCoCrCuFeNi high entropy alloy coatings produced by plasma spraying. *Entropy*. 2013;15:2833-2845.
102. Chen S, Xie X, Li W, et al. Temperature effects on the serrated behavior of an Al0. 5CoCrCuFeNi high-entropy alloy. *Mater Chem Phys*. 2017.210:20–28.
103. Sriharitha R, Murty B, Kottada RS. Phase formation in mechanically alloyed AlxCoCrCuFeNi (x= 0.45, 1, 2.5, 5 Mol) high entropy alloys. *Intermetallics*. 2013;32:119-126.
104. Wang W-R, Wang W-L, Wang S-C, Tsai Y-C, Lai C-H, Yeh J-W. Effects of Al addition on the microstructure and mechanical property of AlxCoCrFeNi high-entropy alloys. *Intermetallics*. 2012;26:44-51.

105. Asthana R. Solidification processing of reinforced metals: Fabrication techniques. *Key Engineering Materials*. Switzerland: Trans Tech Publications Ltd; 1998:6-86.
106. Hansen N. Hall–Petch relation and boundary strengthening. *Scr Mater*. 2004;51:801-806.
107. AlMangour B, Grzesiak D, Yang J. *Effect of Scanning Methods in the Selective Laser Melting of 316L/TiC Nanocomposities*. Germany: Verlag nicht ermittelbar; 2016
108. Tong C-J, Chen M-R, Yeh J-W, et al. Mechanical performance of the Al x CoCrCuFeNi high-entropy alloy system with multiprincipal elements. *Metal Mater Trans A*. 2005;36:1263-1271.
109. Ding C, Cui X, Jiao J, Zhu P. Effects of substrate preheating temperatures on the microstructure, properties, and residual stress of 12CrNi2 prepared by laser cladding deposition technique. *Materials*. 2018;11:2401.
110. Tsai M-H, Tsai R-C, Chang T, Huang W-F. Intermetallic phases in high-entropy alloys: statistical analysis of their prevalence and structural inheritance. *Metals*. 2019;9:247.
111. Liu Y, Chen M, Li Y, Chen X. Microstructure and mechanical performance of AlxCoCrCuFeNi high-entropy alloys. *Rare Metal Mater Eng*. 2009;38:1602-1607.

How to cite this article: Dada M, Popoola P, Mathe N, et al. Process optimization of high entropy alloys by laser additive manufacturing. *Engineering Reports*. 2020;e12252. https://doi.org/10.1002/eng2.12252